CrystEngComm

ROYAL SOCIETY OF CHEMISTRY

PAPER

View Article Online
View Journal | View Issue

Cite this: *CrystEngComm*, 2025, **27**, 38

Optical properties of $[MMim]_2[CuI_3]$ crystals with 0D single-core trigonal planar structures†

Jiali Han,[a] Shujun Zhu,[a] Xinxin Chen,[a] Haichao Zhou,[a] Jianguo Pan *[ab] and Shangke Pan [ab]

Received 29th July 2024,
Accepted 3rd November 2024

DOI: 10.1039/d4ce00750f

rsc.li/crystengcomm

In recent years, lead-free organic–inorganic hybrid zero-dimensional metal halides have attracted considerable attention due to their outstanding optical properties, largely attributed to the confinement of localized metal groups. We report the discovery of a newly structured $[MMim]_2[CuI_3]$ crystal with a distinct $[CuI_3]^{2-}$ trigonal planar structure encapsulated by inert organic $[MMim]^+$ clusters. The structure, composition, and thermal stability of the crystal were analyzed using XRD and TG–DTA. The optical properties of $[MMim]_2[CuI_3]$ crystals were both experimentally measured and theoretically calculated. These crystals exhibit intense broadband orange luminescence with pronounced Stokes shifts and a microsecond-scale fluorescence lifetime decay, primarily due to self-trapped exciton emission. Temperature-dependent fluorescence spectra were also recorded to explore the luminescence mechanism. In summary, these findings highlight the remarkable potential of lead-free $[MMim]_2[CuI_3]$ crystals in advancing optoelectronic applications.

1. Introduction

Organic metal halide hybrids (OMHHs) have gained considerable research interest in the fields of lasers, light-emitting diodes (LEDs), and radiation detectors, owing to their high photoluminescence quantum yield (PLQY), tunable emission spectra, and excellent charge mobility.[1–5] The adjustable structure, chemical composition, and morphology of these materials provide a broad range of functional capabilities.[6] Various luminescent properties are achieved by systematically controlling the dimensionality of the inorganic anionic groups within OMHHs through appropriate combinations of organic halides and metal halides, which can range from 3D to 2D, 1D, and 0D. Generally, the primary luminescent centers are inorganic metals and halide groups, with metals commonly including Pb, Sn, Sb, Cu, and Mn; among these, lead halides have been extensively studied. While lead halides exhibit excellent photovoltaic properties, their inherent drawbacks—such as toxicity, air instability, and optical vulnerability—have limited their practical applications.[7–9] At present, a major area of research focuses on replacing toxic Pb with non-toxic, resource-abundant, environmentally sustainable transition metals, which offer energy-efficient alternatives.[10,11]

Copper has attracted considerable attention for its non-toxicity, low cost, and abundant natural availability. Zero-dimensional copper halide materials, in particular, are of interest due to their metallic polyhedra, which are surrounded by inorganic or large organic groups, facilitating stable exciton complexes and efficient self-trapped exciton emission.[12,13] These materials function as solid-state "host–guest" hybrid systems, where the photoactive metal halide serves as the "guest" embedded periodically in an organic "host" matrix, thereby displaying the photophysical properties characteristic of individual metal halides. They exhibit a long decay lifetime, high photoluminescence quantum efficiency (PLQEs), large Stokes shift, and broadband emission.

The zero-dimensional photoactive centers in copper halide materials are typically island-like structures composed of copper and halide elements, primarily in the form of copper single-core units and clusters derived from these single-core structures. In single-core systems, the zero-dimensional photoactive center of the crystal $(TBA)CuX_2$ (ref. 14) exhibits a linear structure comprising $[CuBr_2]^-$ and $[CuCl_2]^-$ chains. In cluster structures, $(TAP)CuI_2$,[15] $(MA)_4Cu_2Br_6$,[16] and $[Emim]_4[Cu_4I_8]$[17] consist of $[Cu_2I_4]^{2-}$, $[Cu_2Br_6]^{4-}$, and $[Cu_4I_8]^{4-}$ units, respectively, formed through trigonal planar, tetrahedral, and octahedral edge-sharing. Similarly, $(BTMA)_3Cu_3I_6$ (ref. 18) and $(Gua)_3Cu_2I_5$ (ref. 6) are composed of

[a] *School of Material Sciences and Chemical Engineering, Ningbo University, Ningbo, Zhejiang, 315211, China*
[b] *Key Laboratory of Photoelectric Materials and Devices of Zhejiang Province, Ningbo, Zhejiang, 315211, China*

† Electronic supplementary information (ESI) available. CCDC 2287424. For crystallographic data in CIF or other electronic format see DOI: https://doi.org/10.1039/d4ce00750f

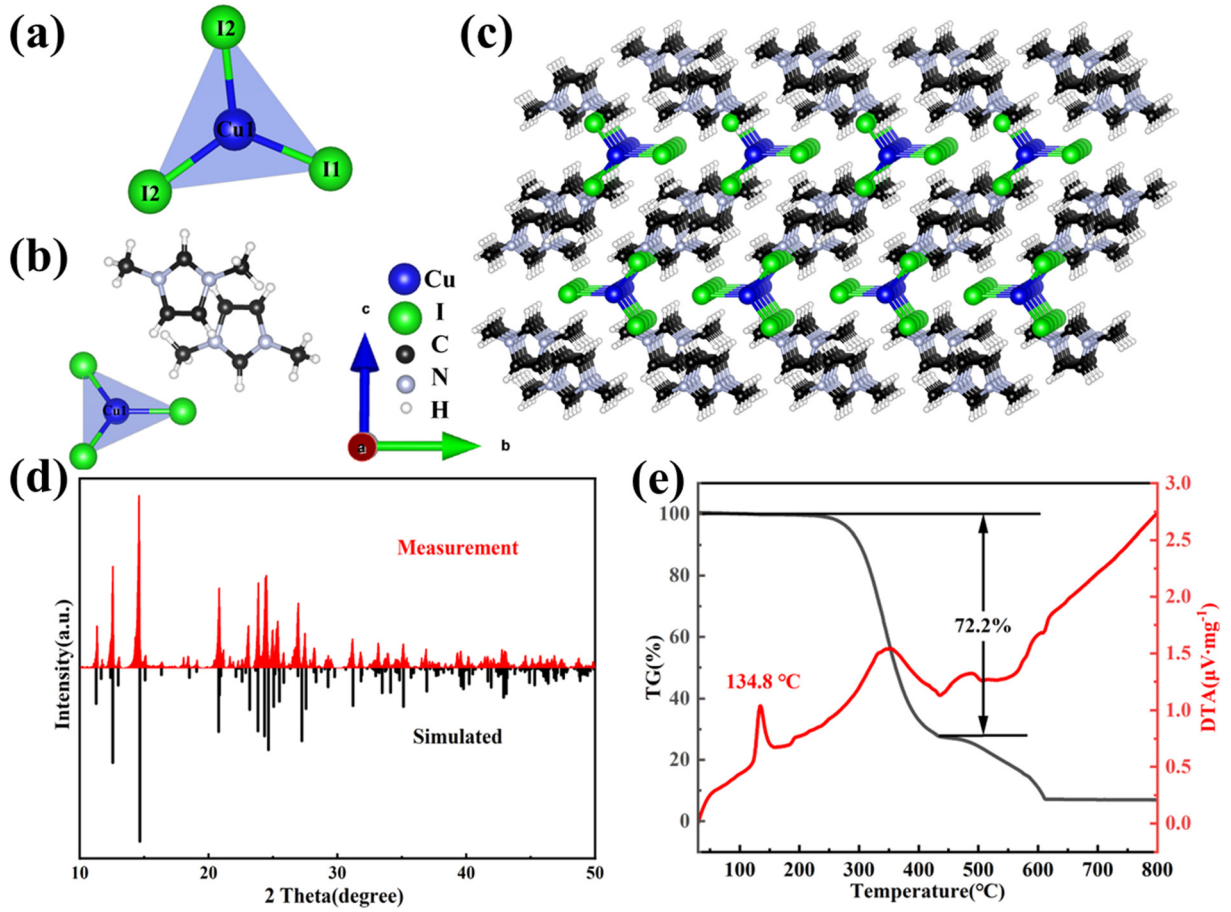

Fig. 1 (a) Connection of Cu and I atoms in a $[CuI_3]^{2-}$ cluster. (b) Asymmetric unit diagram of $[MMim]_2[CuI_3]$. (c) Crystal structure of $[MMim]_2[CuI_3]$, as viewed down the *a* axis. (d) Calculated and experimental X-ray powder patterns of $[MMim]_2[CuI_3]$. (e) The TG–DTA curves of $[MMim]_2[CuI_3]$ single crystals.

$[Cu_3I_6]^{3-}$ and $[Cu_2I_5]^{3-}$ units, formed through trigonal planar and tetrahedral face-sharing arrangements, respectively. Currently, only zero-dimensional linear chain structures have been observed in single-core systems, with no other single-core structures reported.

In this study, a $[MMim]_2[CuI_3]$ (MMim = 1,3-dimethylimidazolium) crystal was synthesized, featuring a novel structure with a single-core trigonal planar $[CuI_3]^{2-}$ unit. Through analysis of its structural and optical properties, several hypotheses were proposed, providing a basis for further investigation into the distinctive characteristics of organic–inorganic hybrid copper halides.

2. Experimental

2.1 Material

1,3-Dimethylimidazolium iodide ([MMim]I, 99.5%) was obtained from the Lanzhou Institute of Chemical Physics, Chinese Academy of Science. Cuprous iodide (CuI, 99.5%) and sodium iodide (NaI, 99.5%) were procured from Shanghai Aladdin Biochemical Technology Co.

The CuI powder was purified *via* recrystallization using an NaI aqueous solution. The primary steps included dissolution, filtration, recrystallization, secondary filtration, vacuum drying, and grinding.

2.2 Single crystal growth

After grinding [MMim]I powder and purified CuI powder in a stoichiometric 2 : 1 ratio in an agate mortar for 30 minutes within a nitrogen-filled glove box (nitrogen mass fraction >99.999% and aqueous oxygen content less than 1.0 ppm), the resulting powder was transferred to a quartz crucible with an 8 mm diameter. The crucible was then removed from the glove box, subjected to heating and vacuum conditions, and subsequently sealed in the ambient atmosphere. The sealed crucible was placed in an oscillating furnace to facilitate thorough melting and mixing of the components. Crystals were then obtained through natural cooling to room temperature.

2.3 Characterization

Testing of $[MMim]_2[CuI_3]$ single crystals was performed on a Bruker D8 VENTURE TXS PHOTON 100 diffractometer at 193 K. The crystal structure was determined using Olex2 software[19] and solved by the SHELXT[20] program through

Table 1 Crystal data of crystals

Complex	$[MMim]_2[CuI_3]$
Empirical formula	$C_{10}H_{18}CuI_3N_4$
Formula weight/(g mol^{-1})	638.52
Temperature/K	193.00
Crystal system	Monoclinic
Space group	$C2/c$
a/Å	8.1644(10)
b/Å	14.9055(16)
c/Å	15.8041(18)
α/°	90
β/°	103.034(4)
γ/°	90
Volume/Å^3	1873.7(4)
Z	4
P_{calc} (g cm^{-3})	2.264
μ/mm^{-1}	6.100
F(000)	1176.0
Crystal size/mm^3	0.13 × 0.12 × 0.10
Radiation	MoKα (λ = 0.71073)
2θ range for data collection/°	5.292 to 61.16
Index ranges	$-11 \le h \le 11$, $-20 \le k \le 21$, $-19 \le l \le 22$
Reflections collected	10 640
Independent reflections	2862 [R_{int} = 0.0474, R_{sigma} = 0.0432]
Data/restraints/parameters	2862/0/85
Goodness-of-fit on F^2	1.028
Final R indexes [$I \ge 2\sigma(I)$]	R_1 = 0.0322, wR_2 = 0.0705
Final R indexes [all data]	R_1 = 0.0406, wR_2 = 0.0757
CCDC	2287424

intrinsic phasing. Structure refinement was conducted with the SHELXL[21] package using least-squares minimization. For powder X-ray diffraction, a Bruker D8 Focus X-ray powder diffractometer with Cu Kα radiation was used at room temperature. The band structure of $[MMim]_2[CuI_3]$ was calculated with VASP software, and the crystal structure was analyzed and optimized using the Perdew–Burke–Ernzerhof (PBE) exchange–correlation functional. Photoluminescence spectra at room temperature were acquired with the F-7100 FL spectrophotometer. Thermogravimetric analysis was conducted using a Netzsch STA 2500C thermogravimetric analyzer in a nitrogen atmosphere. UV-vis absorption spectra were obtained in diffuse-reflectance mode using a Shimadzu UV-3600i spectrophotometer with an integrating sphere. Photoluminescence decay time and PLQY data at room temperature were measured using the FLS-980 steady-state transient fluorescence spectrometer. Additionally, temperature-dependent photoluminescence from 80 to 300 K was collected using the FLS 980.

Table 2 Selected bond lengths (Å) for crystals

Atom–atom	Length/Å	Atom–atom	Length/Å
I2–Cu1	2.5484(4)	N1–C2	1.326(4)
I1–Cu1	2.5191(8)	N1–C3	1.376(4)
N2–C2	1.324(4)	N1–C1	1.460(5)
N2–C4	1.379(4)	C4–C3	1.334(5)
N2–C5	1.467(5)		

Table 3 Selected bond angles (°) for crystals

Atom–atom–atom	Angle/°	Atom–atom–atom	Angle/°
I2–Cu1–I2^a	120.89(3)	C2–N1–C3	108.8(3)
I1–Cu1–I2^a	119.557(14)	C2–N1–C1	124.8(3)
I1–Cu1–I2	119.556(14)	C3–N1–C1	126.3(3)
C2–N2–C4	108.8(3)	N2–C2–N1	108.1(3)
C2–N2–C5	125.0(3)	C3–C4–N2	107.2(3)
C4–N5–C5	126.2(3)	C4–C3–N1	107.2(3)

^{a} $1 - x, +y, 1/2 - z$.

3. Results and discussion

The crystal structure of $[MMim]_2[CuI_3]$ was identified as monoclinic with a $C2/c$ space group and lattice constants of a = 8.1644(10) Å, b = 14.9055(16) Å, and c = 15.8041(18) Å. Fig. 1a–c illustrate the crystal structure of $[MMim]_2CuI_3$, where each Cu atom is coordinated with three I atoms arranged in planar triangles. The isolated $[CuI_3]^{2-}$ clusters are surrounded by $[MMim]^+$ cations, forming a typical 0D framework. The distance between adjacent Cu atoms varies from 8.0365 Å to 8.4975 Å, considerably exceeding half of the van der Waals radius of Cu atoms, thereby indicating the absence of Cu–Cu interactions between $[CuI_3]^{2-}$ clusters.[22] Furthermore, Cu–I bond lengths range from 2.5191 Å to 2.5484 Å, and I–Cu–I bond angles range from 119.556° to 120.89°. This spatial arrangement and separation of $[CuI_3]^{2-}$ clusters by $[MMim]^+$ cations lead to deviations from their ideal trigonal planar configuration. The quantitative distortion of the trigonal planar $[CuI_3]^{2-}$ is calculated to be 2.95×10^{-5} by the distortion of bond lengths $\Delta d = \frac{1}{3}\sum\left(\frac{dn - \overline{d}}{\overline{d}}\right)^2$. Detailed crystal parameters are provided in Tables 1–3.

The powder XRD pattern obtained aligns closely with the calculated single crystal data (Fig. 1d), confirming the sample's purity. TG–DTA analysis (Fig. 1e) shows two stages of weight loss for $[MMim]_2[CuI_3]$ within the range of 20–800 °C. The first stage, corresponding to the loss of [MMim]I, occurs between 240–440 °C and accounts for approximately 72.2% of the total weight loss, which is consistent with the theoretical value of 70.2%. The remaining inorganic framework structure, CuI (ref. 23) decomposes between 430–610 °C. Additionally, $[MMim]_2[CuI_3]$ exhibits a distinct endothermic peak at 134.8 °C, which represents its melting point.

The $[MMim]_2[CuI_3]$ crystals are shown on the left side of Fig. 2a under natural light, with a size of approximately one centimeter. In contrast, the crystals on the right side are exposed to 330 nm UV light, exhibiting a distinct orange luminescence. As depicted in Fig. 2b, these crystals display a clear excitation peak at 360 nm, with a maximum emission peak at 615 nm. The large Stokes shift of 255 nm (1.43 eV) suggests minimal self-absorption. Additionally, the emission peak exhibits a FWHM of 136 nm, with the broad emission profile frequently observed in low-dimensional metal halide

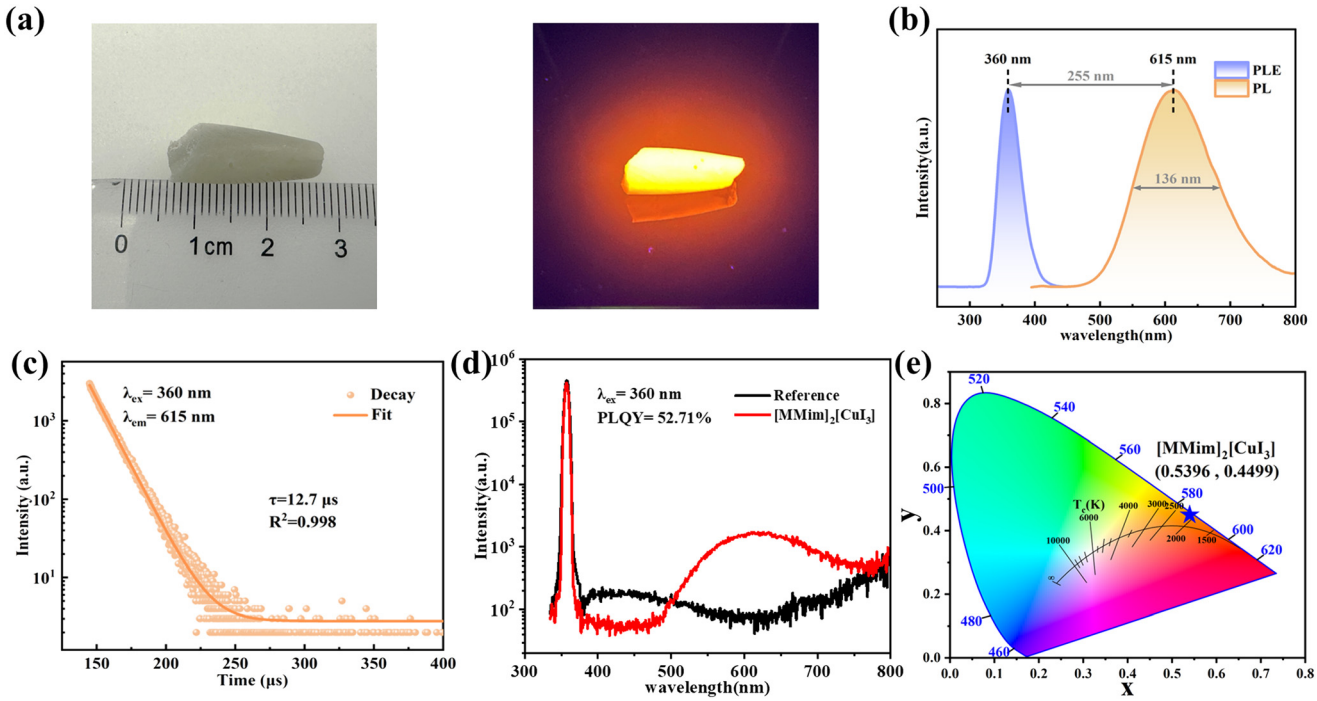

Fig. 2 (a) Photographs of $[MMim]_2[CuI_3]$ single crystals under ambient light (left) and UV light (right) (b) excitation and emission spectra. (c) Time-resolved photoluminescence decay curve. (d) The PLQY spectra. (e) CIE chromaticity diagram of the $[MMim]_2[CuI_3]$ crystals.

hybrids where strong electron–phonon coupling enhances the formation of STEs within the softer lattice, consequently increasing the PLQY.[24] Fig. 2c demonstrates that the PL lifetime decay of $[MMim]_2[CuI_3]$ crystals, measured at room temperature, is well fitted by a single exponential, defined as follows:

$$I(t) = A\exp(-t/\tau)$$

where $I(t)$ is the PL intensity at time t; t refers to the lifetime; and A is constant. The lifetime was determined to be 12.7 μs. The fluorescence lifetime decay of organic–inorganic copper(I) halides is typically in the microsecond range (refer to Table 4). The fluorescence decay of this crystal is relatively fast among similar substances. Fig. 2d shows that the crystals exhibited a PLQY of 52.71% (Table 5). Additionally, the CIE chromaticity coordinates of $[MMim]_2[CuI_3]$, depicted in Fig. 2e, were calculated as (0.5396, 0.4499) based on the PL spectrum, corresponding to an orange luminescence with a color temperature of 2134 K.

Fig. 3a displays the optical absorption spectra of $[MMim]_2[CuI_3]$ crystal powders, revealing a distinct absorption cutoff edge near 350 nm. The band gap was calculated as 3.43 eV using the Tauc equation,[39] aligning with the bandgap of organic–inorganic hybridized cuprous halides (Table 4). The initial absorption feature just below the band gap likely results from excitonic effects, with exciton binding energy slightly lower than the band gap, causing absorption features below the intrinsic band gap of the material. To further examine the optical and electronic properties of

Table 4 Optical parameters of copper-based organic inorganic hybrid halides

Components	PLE/nm	PL/nm	ΔS/nm	Lifetime/μs	Plqy %	E_g/eV	S	E_a	Ref.
$[MMim]_2[CuI_3]$	360	615	255	12.7	52.7	3.55	8.12	87.5	—
$[KC_2]_2[Cu_4I_6]$	400	545	145	2.68	97.8	2.68	—	—	25
$(MA)_4Cu_2Br_6$	302	524	222	120	93	3.87	10.7	—	16
$(TBA)CuCl_2$	286	510	224	28.70	92.8	—	8.46	—	26
$(TBA)CuBr_2$	289	498	209	232.05	80.5	—	14.38	—	26
$(TBA)CuBr_2$	277	511	234	249.4	55	3.92	36.9	—	14
$(C_4H_9)_4NCuCl_2$	282	508	266	28.9	82	3.85	16.2	—	13
$(Gua)_3Cu_2I_5$	325	481	156	1.98	96	2.98	—	77.1	6
$[(C_3H_7)_4N]_2Cu_2I_4$	365	483/637	118/272	3.62/3.67	91.9	3.44	—	—	27
$[Emim]_4[Cu_4I_8]$	334	480	166	69	5.5	3.26	25.2	338.9	17
$(TPA)CuI_2$	365	483/633	122/268	5.25/2.24	84.4	3.47	—	—	15
$(C_{16}H_{36}N)CuI_2$	275	476/675	201/400	6.70/7.65	54.3	—	11.95	994.0	28
$(C_8H_{20}N)_2Cu_2Br_4$	320	468	148	143.6	99.7	4.4	—	—	29

Table 5 Optical parameters of lead-based organic inorganic hybrid halides

Components	PLE/nm	PL/nm	ΔS/nm	Lifetime/μs	Plqy %	E_g/eV	S	E_a	Ref.
$(C_9NH_{20})_7(PbCl_4)Pb_3Cl_{11}$	365	470	122	0.418	83	4.22	—	—	30
$(C_{13}H_{19}N_4)_2PbBr_4$	420	460	40	0.075	44	—	—	—	31
$(TPA)_2PbBr_4$	325/385	437	112/52	0.017	12	3.2	7.098	—	32
$C_4H_{14}N_2PbBr_4$	365	546	181	0.038	18.4	—	22.8	1020	33
$C_5H_{16}N_2Pb_2Br_6$	360	554	194	0.098	10	3.1	—	—	34
[DMEDA]$PbCl_4$	285	565	280	0.048	4.8	—	—	—	35
[BAPrEDA]$PbCl_6{\cdot}(H_2O)_2$,	298	390	92	0.036	21.3	4.69	—	560	36
(EDBE)[$PbCl_4$]	310	538	218	—	2	—	—	—	37
(EDBE)[$PbBr_4$]	371	573	202	—	9	—	—	—	37
(EDBE)[PbI_4]	470	515	45	—	0.5	—	—	—	37
$(2,6\text{-dmpz})_3Pb_2Br_{10}$	—	584	—	0.023	12.24	3.16	—	—	38
$(_4amp)PbBr_4$	—	521	—	0.0025	0.54	—	—	—	38
$(epz)PbBr_4$	—	596	—	0.0027	0.97	—	—	—	38
$(mpz)_2Pb_3Br_{10}$	—	563	—	0.0036	0.33	2.97	—	—	38
$(hmp)PbBr_4$	—	673	—	0.0025	0.46	3.04	—	—	38

$[MMim]_2[CuI_3]$, density-functional theory (DFT) calculations were performed to determine its energy band structure, as shown in Fig. 3b. The intrinsic zero-dimensional nature of the crystal produces an almost flat energy band at the valence band maximum (VBM) and the conduction band minimum (CBM),[39,40] indicating that the electronic states in $[MMim]_2[CuI_3]$ are highly localized, with negligible electronic coupling.[41] This observation highlights the strong quantum confinement effect within the crystal, further suggesting minimal electronic interactions between the $[CuI_3]^{2-}$ clusters. As shown in Fig. 3c and d, the VBM is constituted of Cu 3d and I 5p orbitals, while the CBM consists of N 2p and C 2p orbitals. Due to spatial constraints, electron transitions between the organic and inorganic components are challenging, resulting in direct excitation and transitions within Cu 4s and I 5p orbitals.[17] This phenomenon facilitates STE luminescence within the inorganic clusters, with an E_g of 3.61 eV, consistent with experimental results. Fig. 3e presents emission spectra under different excitations and excitation spectra under various emissions, with both figures exhibiting identical peak shapes and characteristics, suggesting that the crystal's orange luminescence arises from relaxation of the same excited state, ruling out luminescence from other ions. Fig. 3f shows the emission spectra under varying voltages,

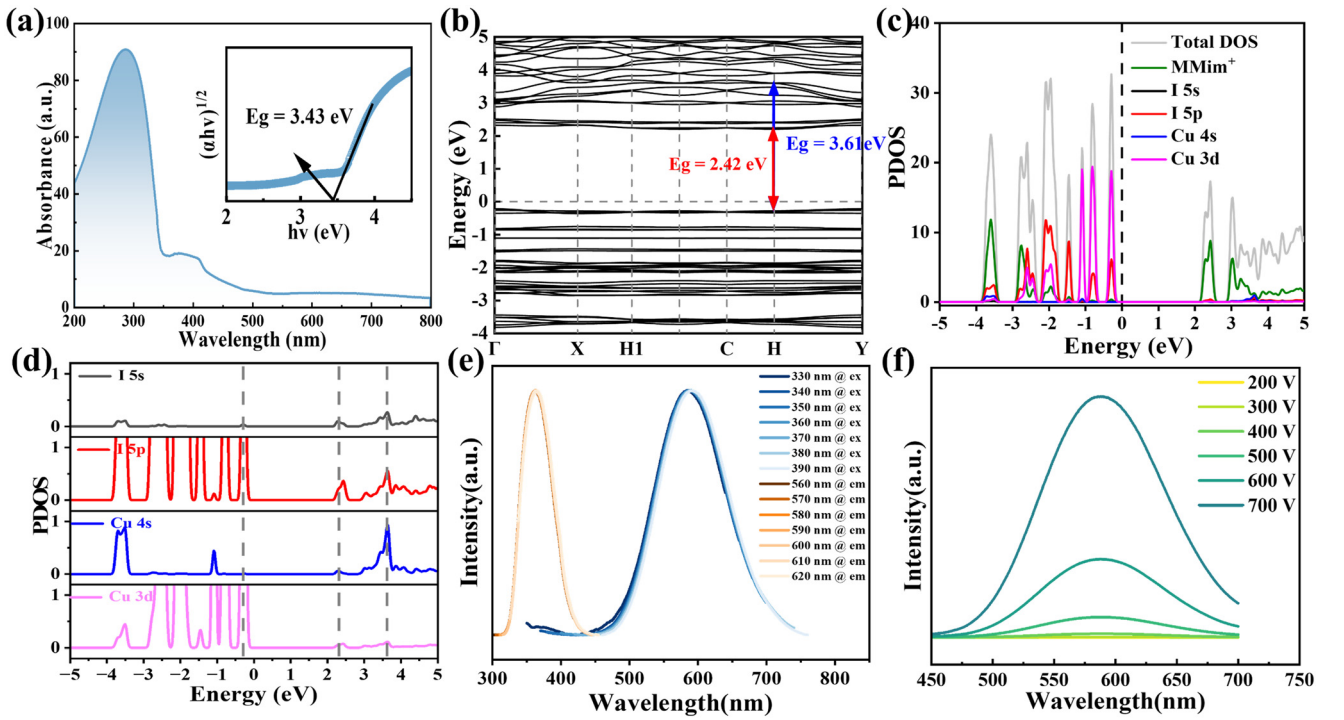

Fig. 3 (a) Absorption spectrum of crystals. The inset shows the band gap of from a Tauc plot. (b) Electronic band structure and (c) PDOS of $[MMim]_2[CuI_3]$. (d) PDOS of the inorganic component in $[MMim]_2[CuI_3]$ (e) emission spectra under different excitations and excitation spectra under different emissions (f) emission spectra under different voltages.

eliminating the possibility of luminescence due to permanent defects.

In investigating the luminescence mechanism of $[MMim]_2[CuI_3]$, we examined its optical properties across different temperatures (Fig. 4a and b). At low temperatures, fluorescence intensity increased with rising temperature, reaching a maximum at 125 K before decreasing with further temperature increases. This trend suggests that the luminescence mechanism of $[MMim]_2[CuI_3]$ is based on STEs emission. Typically, STEs formation involves structural distortions, and there is an energy barrier between free excitons (FEs) and STEs.[42] The structural distortion of the inorganic $[CuI_3]^{2-}$ clusters in the excited state is influenced by the surrounding organic $[MMim]^+$ groups. At low temperatures, the rigidity of the organic framework limits structural deformation, making it challenging for thermal activation energy to convert FEs into self-trapped states. Consequently, most free excitons remain as FEs, resulting in lower luminescence intensity. Between 80–125 K, as temperature increases, the organic groups gain flexibility, allowing thermal activation energy to enable FEs to cross the potential barrier into STEs, thereby increasing fluorescence intensity. However, between 125–325 K, emission intensity declines due to thermal quenching and carrier scattering. This luminescent behavior is illustrated in Fig. 4c. Fig. 4d shows the variation of FWHM and PL peak positions with temperature. The increase in FWHM from 80 K to 325 K is attributed to enhanced electron–phonon interactions, including acoustic phonon and optical longitudinal phonon coupling. Additionally, the observed blue shift in the PL peak position indicates a reduction in electronic coupling with acoustic phonons.[16,43] Moreover, within the temperature range of 80 K to 325 K, fluorescence intensity remains above 72% of its maximum at 125 K, underscoring the remarkable thermal stability of $[MMim]_2[CuI_3]$.

The Huang–Rhys factor, denoted as S, is widely applied to assess phonon–electron coupling, serving as an indicator of electron–phonon interaction strength. The S value of the Huang–Rhys factor plays a critical role in the formation of STE and can be determined through fitting procedures:[2,44]

$$\mathrm{FWHM} = 2.36\sqrt{S}\hbar\omega_{\mathrm{phonon}}\sqrt{\coth\frac{\hbar\omega_{\mathrm{phonon}}}{2k_{\mathrm{B}}T}}$$

where S is Huang–Rhys factor, k_{B} is the Boltzmann constant, $\hbar$ is Planck constant, and ω_{phonon} is phonon frequency. The S factor was calculated to be 8.12 and $\hbar\omega$ phonon to be 61.99 meV. A large S value represents a strong electron–phonon coupling, implying a high degree of lattice structure distortion.[16] The S value of $[MMim]_2[CuI_3]$ is much greater than 1, indicating that it has strong electron–phonon coupling. The role of E_a in the radiative recombination process is crucial. Fig. 4d illustrates the inverse relationship between the Arrhenius integral PL intensity and T (K) temperature (80–325 K), allowing for determination of the

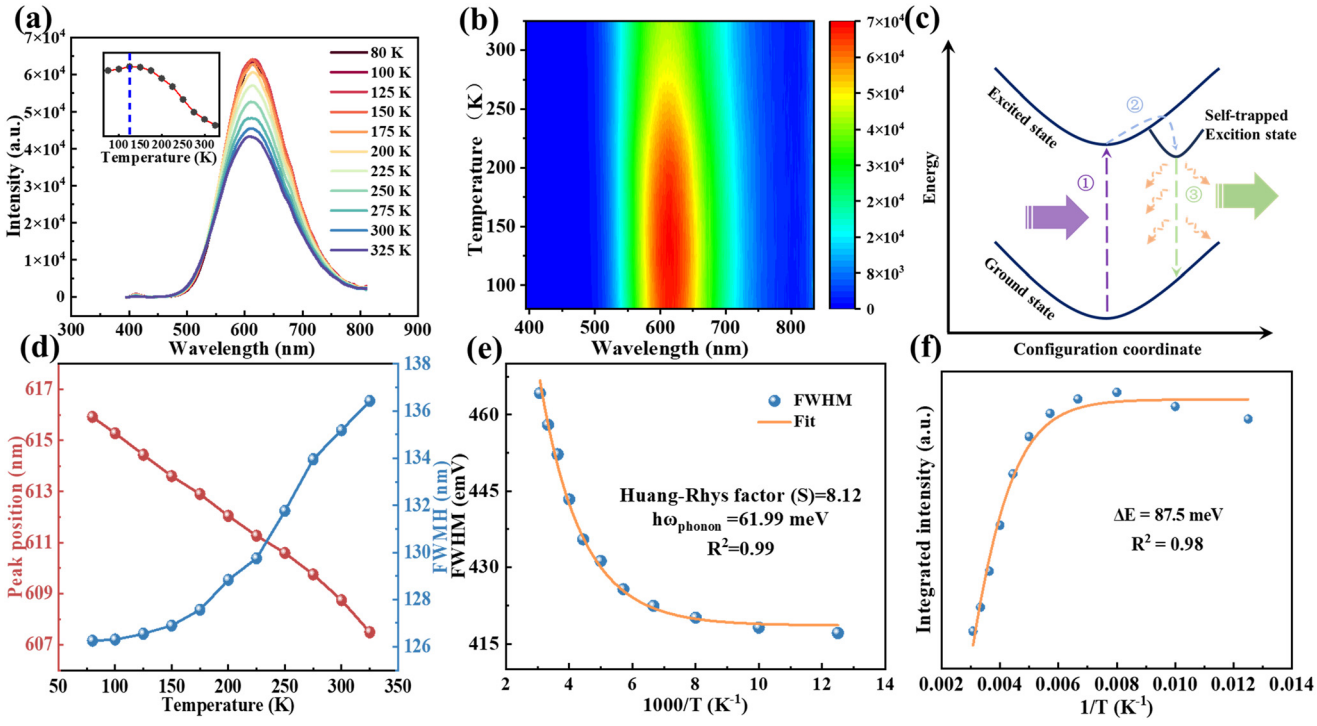

Fig. 4 (a) Temperature-dependent luminescence spectrum for $[MMim]_2[CuI_3]$ crystals. Plot of the maximum PL intensity *vs.* temperature in the upper left. (b) Pseudocolor mapping of variable temperature emission. (c) Schematic illustration of the energy level structure of STE. (d) PL peak position and FWHM varying with temperature (80–325 K). (e) Temperature-dependent FWHM and the fitting curve. (f) Integrated PL intensity as a function of reciprocal temperature (80–325 K).

exciton binding energy.[45,46]

$$I(T) = \frac{I_0}{1 + A\exp\left(-\frac{E_a}{k_B T}\right)}$$

where I_0 is the PL intensity at original temperature; $I(T)$ is the PL intensity at temperature T; A is a constant; k_B is the Boltzmann constant; and E_a expresses the exciton binding energy. The exciton binding energy E_a for $[MMim]_2[CuI_3]$ reaches 87.5 meV, surpassing the thermal energy at room temperature (26 meV (ref. 47)). This high binding energy ensures that $[MMim]_2[CuI_3]$ crystals can efficiently generate and rapidly recombine a substantial number of excitons upon excitation at room temperature, resulting in PL properties. Importantly, these findings provide strong evidence that the observed luminescence in $[MMim]_2[CuI_3]$ originates from exciton recombination rather than free carriers, thereby enhancing our understanding of its optical characteristics.

4. Conclusion

In summary, a novel lead-free copper(I)-based halide crystal, $[MMim]_2[CuI_3]$, has been successfully synthesized, featuring a trigonal planar single-core structure composed of copper and iodine and crystallizing in the monoclinic space group $C2/c$. This crystal has a melting point of 134.8 °C and an estimated optical bandgap of 3.43 eV. The luminescence of $[MMim]_2[CuI_3]$ originates from STEs and displays a broad orange emission peak at 615 nm, with a FWHM of 136 nm, a PLQY of 52.71%, and a PL decay lifetime of 12.7 μs. Interestingly, temperature-dependent analysis indicates that below 125 K, the increased flexibility of organic groups enhances free exciton entry into the STE state, thus intensifying photoluminescence, whereas above 125 K, thermal effects lead to photoluminescence quenching. Additionally, the $[MMim]_2[CuI_3]$ crystal exhibits an exciton binding energy of 87.5 meV and a Huang–Rhys factor of 8.12. In comparison to lead-based materials, the non-toxic properties of this crystal, along with its enhanced photoluminescent characteristics, including a higher PLQY, increase its potential for optoelectronic applications.

Data availability

All relevant data are within the paper.

Author contributions

Jiali Han: conceptualization; methodology; software; validation; investigation; data curation; writing – review & editing; visualization. Shujun Zhu: conceptualization; methodology; formal analysis; writing – review & editing; Xinxin Chen: software; validation; data curation; writing – review. Haichao Zhou: software; validation; investigation; data curation. Jianguo Pan: conceptualization; methodology; data curation; writing – review & editing; supervision; project administration; funding acquisition. Shangke Pan: formal analysis; resources; supervision.

Conflicts of interest

There are no conflicts of interest to declare.

Acknowledgements

This work is partially supported by the National Natural Science Foundation of China (No. 12375180, 61775108), the K. C. Wong Magna Fund in Ningbo University.

References

1 D. Banerjee and B. Saparov, *Chem. Mater.*, 2023, **35**, 3364–3385.
2 Z. Xing, Z. Zhou, G. Zhong, C. C. S. Chan, Y. Li, X. Zou, J. E. Halpert, H. Su and K. S. Wong, *Adv. Funct. Mater.*, 2022, **32**, 2207638.
3 J. Y. Liu, B. Shabbir, C. J. Wang, T. Wan, Q. D. Ou, P. Yu, A. Tadich, X. C. Jiao, D. W. Chu, D. C. Qi, D. B. Li, R. F. Kan, Y. M. Huang, Y. M. Dong, J. Jasieniak, Y. P. Zhang and Q. L. Bao, *Adv. Mater.*, 2019, **31**, 1901644.
4 Q. Wang, X. Wang, Z. Yang, N. Zhou, Y. Deng, J. Zhao, X. Xiao, P. Rudd, A. Moran, Y. Yan and J. Huang, *Nat. Commun.*, 2019, **10**, 5633.
5 Q. Zhao, A. Hazarika, X. Chen, S. P. Harvey, B. W. Larson, G. R. Teeter, J. Liu, T. Song, C. Xiao, L. Shaw, M. Zhang, G. Li, M. C. Beard and J. M. Luther, *Nat. Commun.*, 2019, **10**, 2842.
6 H. Peng, X. Wang, Y. Tian, B. Zou, F. Yang, T. Huang, C. Peng, S. Yao, Z. Yu, Q. Yao, G. Rao and J. Wang, *ACS Appl. Mater. Interfaces*, 2021, **13**, 13443–13451.
7 C. Bi, S. Wang, Q. Li, S. V. Kershaw, J. Tian and A. L. Rogach, *J. Phys. Chem. Lett.*, 2019, **10**, 943–952.
8 X. Gong, O. Voznyy, A. Jain, W. Liu, R. Sabatini, Z. Piontkowski, G. Walters, G. Bappi, S. Nokhrin, O. Bushuyev, M. Yuan, R. Comin, D. McCamant, S. O. Kelley and E. H. Sargent, *Nat. Mater.*, 2018, **17**, 550–556.
9 B. W. Park and S. I. Seok, *Adv. Mater.*, 2019, **31**, 1805337.
10 T. Jun, K. Sim, S. Iimura, M. Sasase, H. Kamioka, J. Kim and H. Hosono, *Adv. Mater.*, 2018, **30**, 1804547.
11 A. M. Elseman, A. E. Shalan, S. Sajid, M. M. Rashad, A. M. Hassan and M. Li, *ACS Appl. Mater. Interfaces*, 2018, **10**, 11699–11707.
12 H. Peng, T. Huang, B. Zou, Y. Tian, X. Wang, Y. Guo, T. Dong, Z. Yu, C. Ding, F. Yang and J. Wang, *Nano Energy*, 2021, **87**, 106166.
13 H. Peng, X. Wang, Y. Tian, T. Dong, Y. Xiao, T. Huang, Y. Guo, J. Wang and B. Zou, *J. Phys. Chem. Lett.*, 2021, **12**, 6639–6647.
14 H. Peng, Y. Tian, Z. H. Zhang, X. X. Wang, T. Huang, T. T. Dong, Y. H. Xiao, J. P. Wang and B. S. Zou, *J. Phys. Chem. C*, 2021, **125**, 20014–20021.
15 L. Lian, S. Wang, H. Ding, G. Liang, Y. B. Zhao, H. Song, X. Lan, J. Gao, R. Chen, D. Zhang and J. Zhang, *Adv. Opt. Mater.*, 2021, **10**, 2101640.

16 H. Peng, S. Yao, Y. Guo, R. Zhi, X. Wang, F. Ge, Y. Tian, J. Wang and B. Zou, *J. Phys. Chem. Lett.*, 2020, **11**, 4703–4710.
17 S. Zhu, J. Pan, X. Chen, H. Chen and S. Pan, *J. Lumin.*, 2023, **253**, 119467.
18 P. Z. L. Lian, J. Gao, D. Zhang and J. Zhang, *Chem. Mater.*, 2023, **35**, 9339–9345.
19 O. V. Dolomanov, L. J. Bourhis, R. J. Gildea, J. A. K. Howard and H. Puschmann, *J. Appl. Crystallogr.*, 2009, **42**, 339–341.
20 G. M. Sheldrick, *Acta Crystallogr., Sect. A: Found. Adv.*, 2015, **71**, 3–8.
21 G. M. Sheldrick, *Acta Crystallogr., Sect. C: Struct. Chem.*, 2015, **71**, 3–8.
22 T. H. Kim, Y. W. Shin, J. H. Jung, J. S. Kim and J. Kim, *Angew. Chem., Int. Ed.*, 2008, **47**, 685–688.
23 F. Liu, P. Hao, T. Yu, Q. Guan and Y. Fu, *J. Mol. Struct.*, 2016, **1119**, 431–436.
24 D. Chen, F. Dai, S. Hao, G. Zhou, Q. Liu, C. Wolverton, J. Zhao and Z. Xia, *J. Mater. Chem. C*, 2020, **8**, 7322–7329.
25 S. Li, J. Xu, Z. Li, Z. Zeng, W. Li, M. Cui, C. Qin and Y. Du, *Chem. Mater.*, 2020, **32**, 6525–6531.
26 L. Lian, X. Wang, P. Zhang, J. Zhu, X. Zhang, J. Gao, S. Wang, G. Liang, D. Zhang, L. Gao, H. Song, R. Chen, X. Lan, W. Liang, G. Niu, J. Tang and J. Zhang, *J. Phys. Chem. Lett.*, 2021, **12**, 6919–6926.
27 H. Peng, Y. Tian, X. X. Wang, T. Huang, Z. M. Yu, Y. T. Zhao, T. T. Dong, J. P. Wang and B. S. Zou, *ACS Appl. Mater. Interfaces*, 2022, **14**, 12395–12403.
28 L. Lian, P. Zhang, G. Liang, S. Wang, X. Wang, Y. Wang, X. Zhang, J. Gao, D. Zhang, L. Gao, H. Song, R. Chen, X. Lan, W. Liang, G. Niu, J. Tang and J. Zhang, *ACS Appl. Mater. Interfaces*, 2021, **13**, 22749–22756.
29 B. Su, J. Jin, K. Han and Z. Xia, *Adv. Funct. Mater.*, 2022, **33**, 2210735.
30 C. Zhou, H. Lin, M. Worku, J. Neu, Y. Zhou, Y. Tian, S. Lee, P. Djurovich, T. Siegrist and B. Ma, *J. Am. Chem. Soc.*, 2018, **140**, 13181–13184.
31 H. Lin, C. Zhou, M. Chaaban, L.-J. Xu, Y. Zhou, J. Neu, M. Worku, E. Berkwits, Q. He, S. Lee, X. Lin, T. Siegrist, M.-H. Du and B. Ma, *ACS Mater. Lett.*, 2019, **1**, 594–598.
32 Y. Tian, Q. Wei, H. Peng, Z. Yu, S. Yao, B. Ke, Q. Li and B. Zou, *Nanomaterials*, 2022, **12**, 2222.
33 H. Peng, Y. Tian, X. Wang, S. Yao, T. Huang, Y. Guo, L. Shi and B. Zou, *New J. Chem.*, 2021, **45**, 17247–17257.
34 H. Lin, C. Zhou, J. Neu, Y. Zhou, D. Han, S. Chen, M. Worku, M. Chaaban, S. Lee, E. Berkwits, T. Siegrist, M. H. Du and B. Ma, *Adv. Opt. Mater.*, 2019, **7**, 594–598.
35 C. Sun, Y.-D. Yue, W.-F. Zhang, X.-Y. Sun, Y. Du, H.-M. Pan, Y.-Y. Ma, Y.-C. He, M.-T. Li and Z.-H. Jing, *CrystEngComm*, 2020, **22**, 1480–1486.
36 C. Sun, K. Jiang, M.-F. Han, M.-J. Liu, X.-K. Lian, Y.-X. Jiang, H.-S. Shi, C.-Y. Yue and X.-W. Lei, *J. Mater. Chem. C*, 2020, **8**, 11890–11895.
37 E. R. Dohner, A. Jaffe, L. R. Bradshaw and H. I. Karunadasa, *J. Am. Chem. Soc.*, 2014, **136**, 13154–13157.
38 L. L. Mao, P. J. Guo, M. Kepenekian, I. Hadar, C. Katan, J. Even, R. D. Schaller, C. C. Stoumpos and M. G. Kanatzidis, *J. Am. Chem. Soc.*, 2018, **140**, 13078–13088.
39 D. Chen, S. Hao, G. Zhou, C. Deng, Q. Liu, S. Ma, C. Wolverton, J. Zhao and Z. Xia, *Inorg. Chem.*, 2019, **58**, 15602–15609.
40 J. P. Perdew and M. Levy, *Phys. Rev. Lett.*, 1983, **51**, 1884–1887.
41 C. Zhou, H. Lin, H. Shi, Y. Tian, C. Pak, M. Shatruk, Y. Zhou, P. Djurovich, M. H. Du and B. Ma, *Angew. Chem.*, 2017, **130**, 1033–1036.
42 M. D. Smith, A. Jaffe, E. R. Dohner, A. M. Lindenberg and H. I. Karunadasa, *Chem. Sci.*, 2017, **8**, 4497–4504.
43 R. Saran, A. Heuer-Jungemann, A. G. Kanaras and R. J. Curry, *Adv. Opt. Mater.*, 2017, **5**, 1700231.
44 Z. Ma, Z. Shi, C. Qin, M. Cui, D. Yang, X. Wang, L. Wang, X. Ji, X. Chen, J. Sun, D. Wu, Y. Zhang, X. J. Li, L. Zhang and C. Shan, *ACS Nano*, 2020, **14**, 4475–4486.
45 Y. Lu, S. Fang, G. Li and L. Li, *J. Alloys Compd.*, 2022, **903**, 163924.
46 F. Zhang, Z. Zhao, B. Chen, H. Zheng, L. Huang, Y. Liu, Y. Wang and A. L. Rogach, *Adv. Opt. Mater.*, 2020, **8**, 1901723.
47 J. Zhang, Y. Yang, H. Deng, U. Farooq, X. Yang, J. Khan, J. Tang and H. Song, *ACS Nano*, 2017, **11**, 9294–9302.